Fiber-Drawn Metamaterial for THz Waveguiding and Imaging

Atakaramians, Shaghik; Stefani, Alessio ; Li, Haisu; Habib, Md. Samiul; Hayashi, Juliano Grigoleto; Tuniz, Alessandro; Tang, Xiaoli; Anthony, Jessienta; Lwin, Richard; Argyros, Alexander

Total number of authors:
12

Published in:
Journal of Infrared, Millimeter and Terahertz Waves

Link to article, DOI:
10.1007/s10762-017-0383-0

Publication date:
2017

Document Version
Peer reviewed version

Fiber drawn metamaterial for THz waveguiding and imaging

Shaghik Atakaramias[1*], Alessio Stefani[1,2*], Haisu Li[1,3], Md. Samiul Habib[1], Juliano Grigoleto Hayashi[1], AlessandroTuniz[1], Xiaoli Tang[1], Jessienta Anthony[1], Richard Lwin[1], Alexander Argyros[1], Simon C. Fleming[1], Boris T. Kuhlmey[1,4]

1. Institute of Photonics and Optical Science, School of Physics, The University of Sydney, Sydney NSW 2006, Australia
2. DTU Fotonik, Department of Photonics Engineering, Technical University of Denmark, DK-2800 Kgs. Lyngby, Denmark
3. Key Laboratory of All Optical Network and Advanced Telecommunication Network of EMC, Institute of Lightwave Technology, Beijing Jiaotong University, Beijing 100044, China
4. Centre for Ultrahigh Bandwidth Devices for Optical Systems (CUDOS), the University of Sydney, New South Wales 2006, Australia

Email: shaghik.atakaramians@sydney.edu.au

* These authors contributed equally to this work.

Abstract In this paper we review the work of our group in fabricating metamaterials for terahertz (THz) applications by fiber drawing. We discuss the fabrication technique and the structures that can be obtained before focusing on two particular applications of terahertz metamaterials, i.e. waveguiding and sub-diffraction imaging. We show the experimental demonstration of THz radiation guidance through hollow core waveguides with metamaterial cladding, where substantial improvements were realised compared to conventional hollow core waveguides, such as reduction of size, greater flexibility, increased single mode operating regime and guiding due to magnetic and electric resonances. We also report recent and new experimental work on near- and far-field THz imaging using wire array metamaterials that are capable of resolving features as small as λ/28.

Keywords: metamaterials, terahertz, waveguide, imaging, wire array, fiber drawing

1. Introduction

Work at THz frequencies, loosely defined as 0.1 to 10 THz in frequency or 3 mm to 30 μm in wavelength, has been rapidly increasing due to the relatively recent availability of affordable and practical THz sources and detectors, bridging the so-called "THz gap" which had previously resulted in this part of the spectrum being under-utilized, see for example [1]. THz radiation is very attractive for numerous applications including short-range wireless communication, imaging, chemical and biological spectroscopy and sensing, material characterization, as well as security, see for example [2-5]. The foremost challenge for exploiting THz radiation is the lack of materials offering a suitable THz electronic response. Metamaterials have sparked an exciting opportunity for manipulating THz waves beyond what is possible with natural materials [6,7].

Metamaterials are man-made composites with structure on a subwavelength scale, where the arrangement of the subwavelength features defines the permittivity and permeability [8]. Hence, metamaterials' control over the permittivity and permeability can provide extraordinary functionalities not available with naturally occurring materials, such as cloaking, sub-diffraction imaging, and sub-wavelength confinement [9-11]. The ability to control radiation on scales comparable to, or smaller than the wavelength makes metamaterials of particular interest in the THz region allowing a further boost to THz technology and development.

Fabrication of metamaterials is considered easier at microwave wavelengths, as the lattice constant is on the order of millimeters. However, at THz and shorter wavelengths, it becomes challenging as the dimensions become micro- and nano-scale. A decade ago, most THz metamaterials were limited to two dimensional geometries (also known as metasurfaces) and fabricated using photolithography [7]. Since then, new fabrication techniques such as stereolithography (3D printing) [12], inclined X-ray lithography and project lithography [13,14] or self-organization [15] have been proposed, enabling the manufacture of THz metamaterials. Over recent years we have pioneered the use of fiber drawing to realize longitudinally invariant 3D metamaterials.

Fiber drawing of metamaterials, inspired from optical fiber drawing, is an efficient fabrication technique to realize THz metamaterials: it allows great control in scalability and has the potential for mass production because of the ease of manufacturing large quantities. Using this technique, we have successfully achieved the fabrication of arrays of two quintessential meta-atoms: wire arrays which give control over the permittivity, and split-ring-resonators - similar to LC circuits with a magnetic resonance - to tailor the permeability. Based on these two meta-atoms, the responses of THz metamaterials have been characterized, and corresponding novel devices, including hollow core waveguides for THz wave guidance and imaging probes for focusing and magnification, have been demonstrated. In this review, we focus on the fiber drawn metamaterials based THz waveguides and imaging applications we have recently demonstrated.

This review is organized as follows. In Section 2, we describe and discuss the fiber drawing method to fabricate THz metamaterials. Section 3 presents three kinds of THz waveguides with metamaterial cladding. In Section 4 we review and report new results on the subwavelength imaging technologies using straight and tapered wire array metamaterials at THz frequencies. Finally, the conclusion and outlook are presented in Section 5.

2. Fiber drawing of metamaterials

Fiber drawing enables the fabrication of structures with a cross-sectional pattern that extends for very long lengths. The idea of using fiber drawing for metamaterials naturally emerged from the combination of well-developed techniques: stack-and-draw (or drill-and-draw) procedures routinely used in the production of photonic crystal fibers, and the Taylor wire process. Photonic crystal fibers (or microstructured fibers) are optical fibers with guidance properties determined by air holes properly arranged in the fiber cross-section. They were first realized in fibers made of fused silica [16], and subsequently in polymer fibers [17]. The Taylor wire process [18,19] is a technique that was developed to fabricate glass coated microwires. In this technique a glass tube containing molten metal is drawn to reach the desired size. We have exploited a combination of the Taylor wire process with fiber-preform micro-structuring first pioneered by the University of Bath in a different context [20] to fabricate fibers with novel and extreme electromagnetic properties, e.g. indefinite media.

The fabrication process relies on the plastic deformation of a macroscopic reproduction of the desired structure. The initial structure in its macroscopic form is called a preform and it can be created by stacking tubes, by drilling into bulk materials, by casting, by extrusion [17,21] or by 3D printing [22]. The preform is placed vertically in a furnace and heated above the glass transition temperature, where it can be deformed.

Controlling the ratio between the velocity at which the preform is fed into the furnace and that at which it is pulled out, it is possible to control the size of the final product. Multiple drawing stages can be used when necessary. This process allows for easy scalability and mass production of the structures.

The standard host materials used are polymers, which have drawing temperatures between 150 and 200 ˚C including Poly-methyl methacrylate (PMMA), Cyclic-Olefin polymer (Zeonex®), Polycarbonate (PC) and Polyurethane (PU). Some of these are very interesting at THz frequencies because of their material attenuation and dispersion, others because of their mechanical properties.

The simplest metamaterial structure that can be realized by fiber drawing is a wire array. The presence of subwavelength wires substantially affects the permittivity tensor components along and across the wire. Along the wires, the metamaterial's effective permittivity can be described by a non-local Drude model, taking negative values below a plasma frequencies that depends on wire spacing and diameter, and can readily designed to be in the THz range. In the direction perpendicular to the wires, the permittivity typically remains positive, so that the overall permittivity tensor can be indefinite [23], leading to hyperbolic dispersion relations and unusual properties including increased density of states and the ability to beat the diffraction limit [24]. Wire arrays can be fabricated by stacking multiple tubes, each enclosing a metal wire. In order to combine fiber drawing with the Taylor wire process, the metal must have a melting temperature lower than the drawing temperature of the enclosing dielectric. Given the choice of polymer host materials and their glass transition temperature, there are not many compatible metals. One of them is indium, which has a melting temperature of 156.6˚C; it has been used in combination with the various polymers for the work reported here. There are two ways to obtain a metal filled tube: by infiltrating molten metal in an empty tube or by a first drawing step where a solid wire is inserted in a tube, prior to the drawing, and melts during the stretching process [25-27]. By taking advantage of the fiber drawing process it was possible to scale the wire arrays down by a few orders of magnitude and thus realize structures with as many as 500 wires. The minimum achievable wire size was limited by the Plateau-Rayleigh instability [28], which is responsible for the liquid wires breaking into droplets. For the specific combination of PMMA and indium, and considering the restrictions in terms of temperature and tension due to the drawing process, this limit is reached for wires of a few micrometers in diameter. With this process, long uniform sections of wire arrays can be obtained, some examples of which are shown in Fig. 1(a). The ability to control the permittivity was demonstrated by measuring the transition between metallic and dielectric behavior (physically expressed by the plasma frequency, which indicates the frequency at which the permittivity of the material is 0) of the wire arrays and its dependence on the structure's dimensions with THz time domain spectroscopy (TDS), Fig. 1(b) [25]. At low frequency the wire array behaves like a metal and therefore the transmission is low. The transmission, in a logarithmic scale, increases linearly with frequency as the (negative) permittivity increases and therefore the tunneling through the "metal" increases. As the permittivity approaches in absolute value that of the polymer jacket, the transmission is no more trivial and is the result of a combination of change in permittivity, electrostatic and geometric resonances, and material loss (more details in [25]). While the plasma frequency cannot easily be recognized from the transmission curves, it is clear that the metallic to dielectric transition is shifted to higher frequencies when scaling the structure. All

the transmission measurement presented in this work are normalized to the free space transmission of the TDS system. Uniform structures are not the only ones that this technique can be used to fabricate. In fact, it is possible to take advantage of the transition region of the drawing process to also realize tapered structures [29].

Wire arrays allow engineering of the material electric permittivity. In order to also control the magnetic permeability, a magnetic response is required, which in metamaterials is canonically achieved using split-ring resonators (SRRs). Whilst surface tension does not deform the circular geometry of simple wires, split-ring resonators are less straightforward to fabricate using fiber drawing techniques. However, by optimizing drawing temperature and speed we demonstrated the fabrication of both single [30] and double [31] resonator structures by fiber drawing. The cross-sections of some of the SRR are shown in Fig. 2(a) and (c), while the presence of a magnetic resonance is shown in Fig. 2(b), as measured by THz TDS. The ability to control both permittivity and permeability opens a pathway to realisation of the most attractive aspects of metamaterials, such as negative refraction, perfect lensing and invisibility.

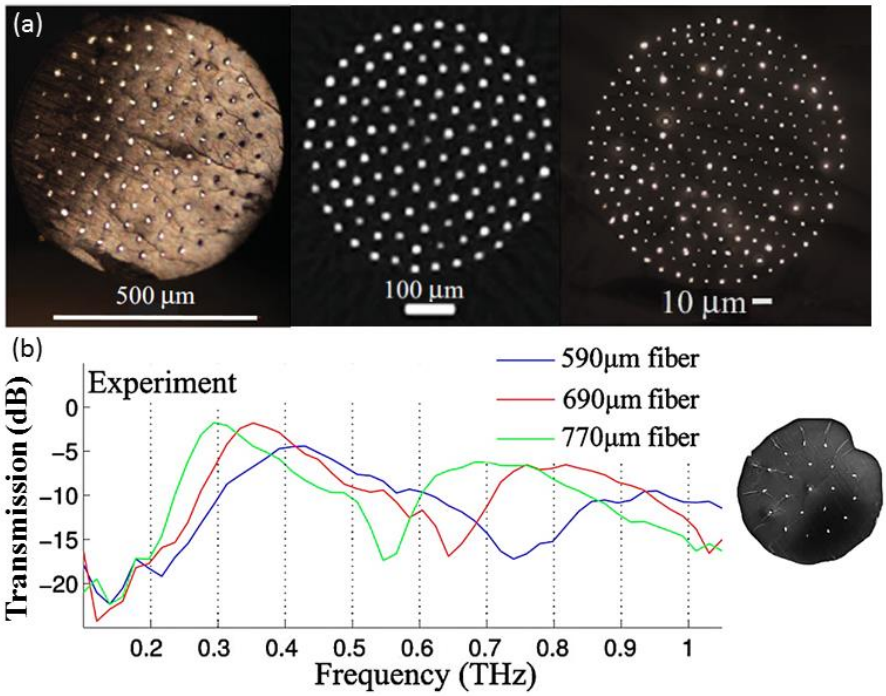

Fig. 1 (a) Cross-section of fabricated wire arrays in various dimensions [26]. (b) THz TDS transmission, showing a high pass filter-like curve indicating the transition between metallic and dielectric behaviour, for different scaling of the wire array [25].

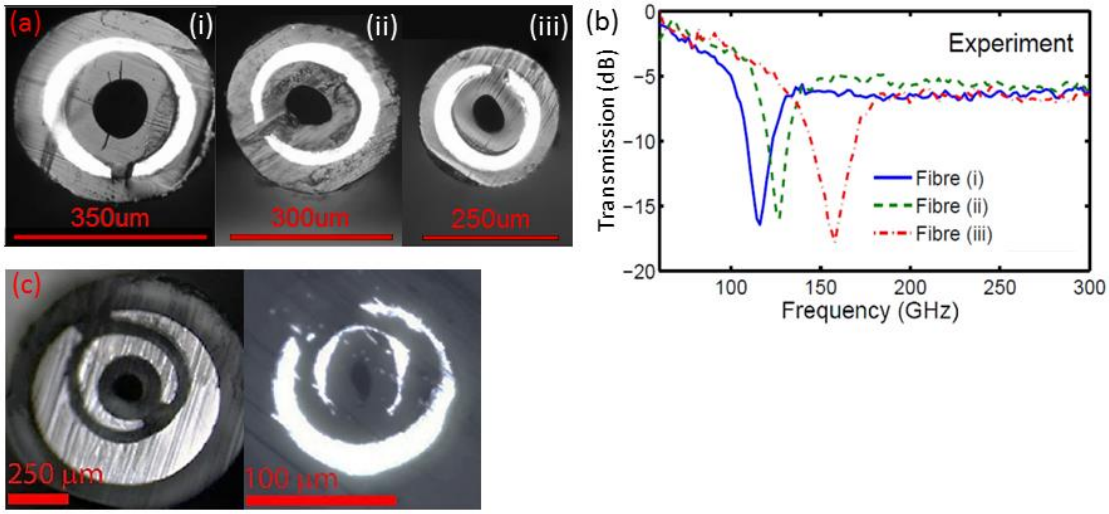

Fig. 2 Cross-section of fabricated split-ring resonators in various dimensions: (a) single [30], (c) double [31]. (b) THz TDS transmission, showing the magnetic resonance, for the SRRs in (a) [31].

An alternative approach to realizing metamaterials with a magnetic response which makes use of fiber drawing but does not make use of the Taylor wire process is to sputter a spool of fully dielectric rods/fibers with metal and obtain ridge u-shaped metal structures [32,33].

2.1 Tunable metamaterials

Metamaterials fabricated by fiber drawing typically result in a rigid dielectric structure with fixed refractive index, making subsequent tuning of the electromagnetic properties difficult. Adding air holes to the structure could be a first solution to this problem, where tunability is achieved by filling the air holes with liquids of various refractive indices. However, few liquids have sufficiently low losses at THz frequencies. We instead explored the increased deformability air holes provide: applying lateral pressure deforms the structure (as well as the average refractive index). Despite the apparent advantages of this design, the polymer we used, PMMA, did not allow reversible tuning [34].

In order to achieve a structural tuning which is reversible, we followed a different approach, using a dielectric matrix that has a much lower Young's modulus. We therefore investigated the possibility of fiber drawing a wire array with PU as host [34]. Polyurethane can have a Young's modulus almost three orders of magnitude lower than PMMA and a breaking strain larger than 600% [35]. The realized wire array is shown as an inset in Fig. 3. The transmission through a 1 cm square planar sample of such wire array metamaterials, placed between two Zeonex plates, was measured with THz TDS. A clear transition from low to high transmission shows the metallic to dielectric transition of the wire medium [Fig. 3]. Compression and release experiments demonstrated tuning of this transition by 200 GHz, equivalent to 50% of the initial value, in a reversible and repeatable manner. Prior to this demonstration, different structures with various sizes were required to modify the plasma frequency, for example, reported in Fig. 1(b), however this was fixed at

fabrication time and not subsequently or dynamically tunable.

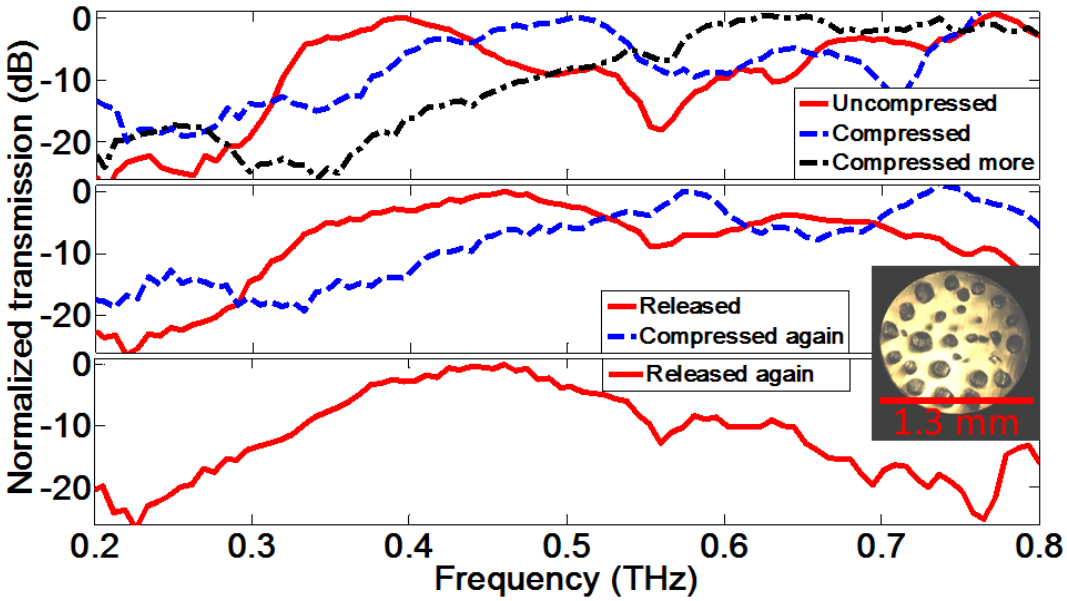

Fig. 3 THz TDS transmission through the wire array during cycles of compression and release. Inset: fabricated PU wire array [34].

2.2 Towards the Infrared

As already mentioned, the length scales over which continuous metal wires with micro-scale diameters can be achieved using polymers and indium are in practice limited by the Rayleigh instability,. In order to fabricate continuous sub-wavelength wire structures for operation at frequencies above 3 THz or even the near infrared (IR), materials with lower surface tension or higher tensile strength are necessary. For this purpose, glasses represent a suitable class of host materials. In particular, soft-glasses with lower glass transition temperatures compared to fused silica are a favorable type of low processing temperature material. An interesting soft glass is soda-lime glass as it is low cost, easy to process, and its transmission extends almost to 3 µm. The drawback of soda-lime comes from its high material loss. However, when considering the size of metamaterial devices, the material loss is almost negligible. We investigated the compatibility between drawing parameters and optical properties of various metals [36]. From the investigation, tin was determined to be the preferred metal to be included in soda-lime glass in order to realize wire arrays operating in the 3 µm wavelength region. Recently, we demonstrated a wire array with ~500 metal wires with diameters down to 300 nm and the ability to taper such structures in order to fabricate hyperlenses out of this wire medium [37]. Images of the cross-section of the wire medium and of a taper are shown in Fig. 4.

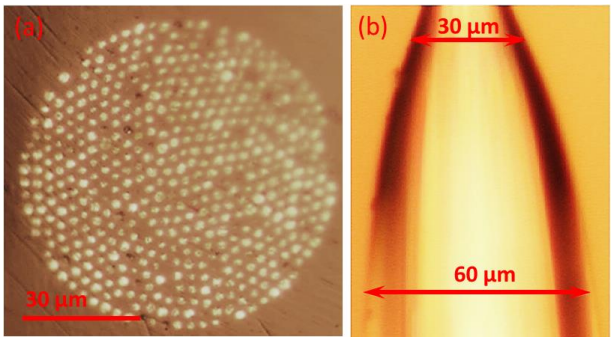

Fig. 4 (a) Cross-section of tin/soda-lime glass wire array. (b) Tapered tin/soda-lime glass wire array [37].

3 Hollow core waveguides with metamaterial cladding

A key requirement to achieve compact THz devices is a strongly confining single mode and low loss waveguide. Several waveguide solutions based on technologies from both electronics and photonics have been proposed [38-42]; among these hollow core waveguides are one of the best options for guiding THz radiation due to the very low material absorption of air. However, hollow core waveguides suffer from multimode operation as they have a core diameter larger than the operating wavelength to minimize reflection losses [43-47]. Metamaterials offer a new paradigm to reduce the number of modes due to their unusual optical properties [48, 49]. A theoretical investigation, aiming at lowering losses of large core IR fibers, by Yan and Mortensen showed that wire based metamaterials could provide guidance to transverse magnetic (TM) modes [50]. Motivated by their work, we have developed a fully analytical model for modal analysis (the characteristic equation for guided modes and relevant mode existence condition) of hollow core waveguides with uniaxial metamaterial cladding [48,49]. This study enables us to discover many other interesting and unusual properties of highly anisotropic metamaterial clad waveguides, such as various regimes of subwavelength confinement and guidance due to magnetic and electric resonances, which was also subsequently studied for solid core waveguides with metamaterial cladding [11]. We also showed that waveguides with uniaxial anisotropic cladding can be used to create subwavelength dimension cavities [51]. Here, we summarize our recent experimental demonstrations of THz hollow core waveguides with metamaterial cladding.

3.1 Hollow core flexible THz waveguide with wire metamaterial cladding

We have reported a single mode single polarization hollow core THz fiber with a metamaterial cladding, consisting of subwavelength diameter metal wires embedded in a dielectric host [52,53]. Our numerical studies revealed that a single layer of metal wires in the cladding could confine more than 95% of the power in the air-core, with performance similar to that of a hollow core waveguide surrounded by an infinite wire metamaterial (WMM) cladding. Figure 5 shows the schematic [Fig. 5(a)], image of fabricated flexible fiber [Fig. 5(b)] and microscope image of the cross-section [Fig. 5(c)] of the waveguide. We used a standard THz TDS system to investigate the transmission properties of the THz radiation through the fiber. We blocked half of the fiber input

end face with a metallic tape in order to excite TM or TE mode using a linearly polarized THz wave, as shown in Figs. 6(a) and 6(b).

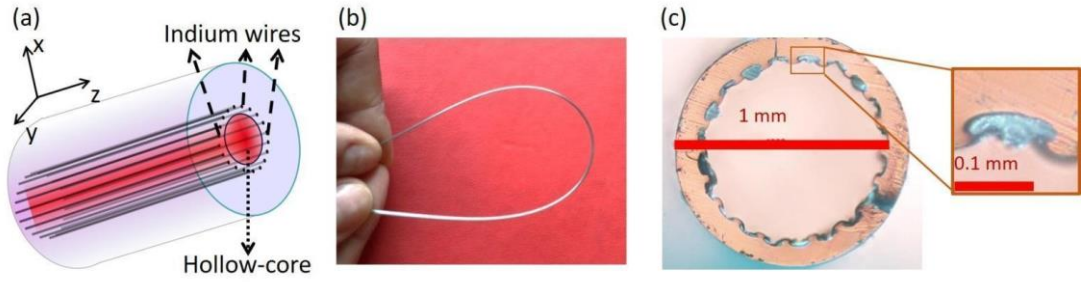

Fig. 5 (a) Schematic, (b) photograph of fabricated and (c) microscope image of the cross-section of hollow core metamaterial clad waveguide. The inset image in part (c) shows one of the indium wires [53].

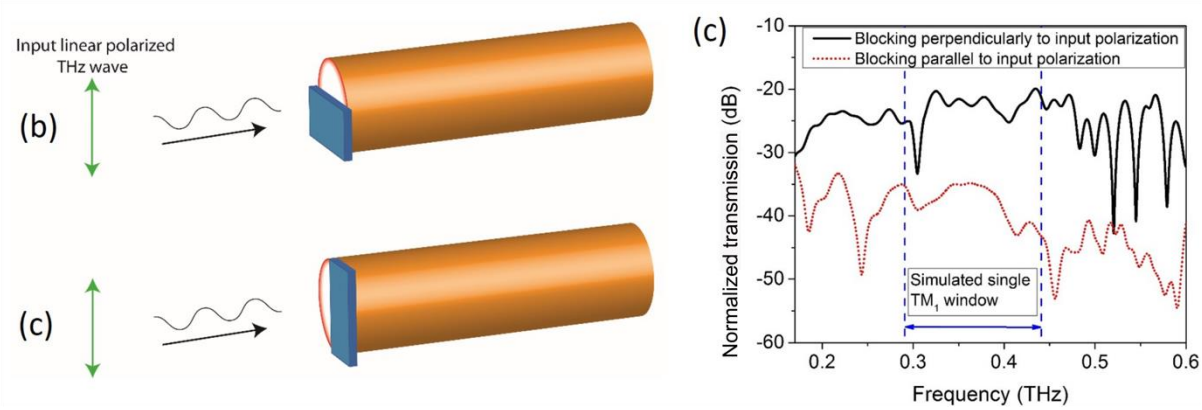

Fig. 6 Experimental configurations coupling into (b) TM modes (perpendicular blocking) and (c) TE mode (parallel blocking) with respect to input linearly polarized THz wave. (c) Comparison of normalized transmissions between TM (black solid curve) and TE (red dotted curve) modes [53].

The normalized transmission spectra with the two configurations of tapes are presented in Fig. 6(c). Considerable high TM-only transmission was observed when the waveguide input was blocked perpendicularly to the polarization of the input THz wave [black solid curve in Fig. 6(c)] compared to when the waveguide input was blocked parallel to the polarization [red dotted curve in Fig. 6(c)]. Three distinct regions are visible in the case of TM excitation. At high frequencies (above 0.44 THz) multimode propagation is seen in the form of multiple peaks and dips due to modal beating. Between 0.31 THz and 0.44 THz, a relatively high and smooth transmission was observed consistent with the propagation of single, pure first order TM mode (TM_1). Both experimental and theoretical studies confirm a single mode bandwidth 2.3 times wider than that of dielectric-coated metallic waveguide with the same core dimension. The normalized near-field modal profile at 0.31 [Fig. 7(a)] was in excellent agreement with the simulated profile [Fig. 7(b)], further confirming the radially-polarized single mode TM_1 propagation in our waveguide. Surprisingly, there was non-zero transmission also in the region 0.2-0.3 THz [Fig. 6(c)]. Further studies revealed that this transmission was due to the existence of surface

plasmon polariton-like (SPP) modes [49], which was confirmed by the normalized near-field modal distribution profile at the core-cladding interface at 0.23 THz [Figs. 7(c) and 7(d) show measured and simulated images, respectively]. Additionally, by symmetrically removing a few of the metal wires with respect to the *x*-axis of the proposed structure, the metamaterial cladding fiber could provide linearly polarized (electric vector along *x*-axis) single TM mode transmission [54].

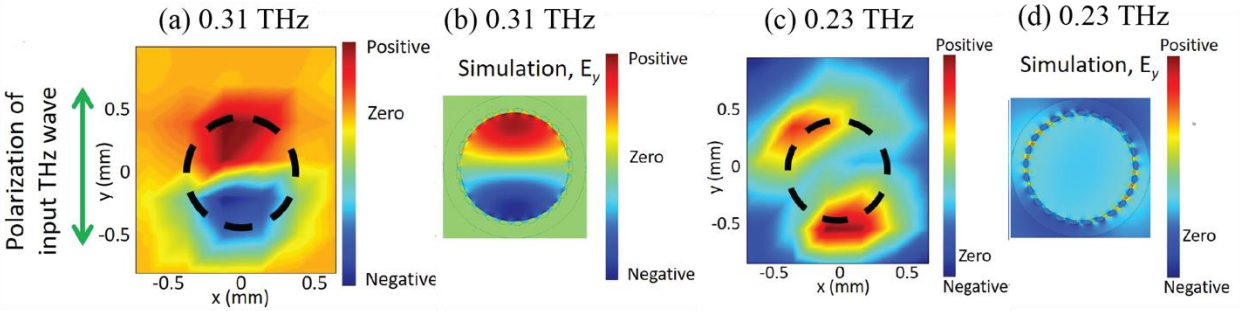

Fig. 7 Measured normalized near-field modal profiles of fabricated waveguide at (a) 0.31 THz and (c) 0.23 THz. The polarization of THz source and detector is shown by green arrow on the left. (c) Simulated *y*-component of modal electric field at (b) 0.31 THz and (d) 0.23 THz [53].

3.2 Hybrid antiresonant metamaterial waveguides

A slightly different approach to exploiting the properties of an indefinite wire array cladding can be taken by combining an antiresonant guiding structure and a metamaterial cladding [55]. Antiresonant structures allow guidance in a region with lower refractive index than the surrounding material when the surrounding material is sufficiently thin. Light can couple out only when constructive interference occurs within the thin layer [56]. This guiding mechanism allows for broadband guidance in simple hollow structures. Recently, it was demonstrated that using an hypocycloidal core (achieved by a ring of capillaries) can greatly reduce the guiding loss of antiresonant structures [57]. These structures have therefore been investigated in an attempt to achieve low loss guidance also for THz frequencies [58-59], but it is very challenging to fabricate the thin core wall structures with the required accuracy.

As shown in the previous section, a ring of metal wires around the core allows guidance in a hollow core for a specific mode and for a certain bandwidth [53]. The same concept could be scaled to a larger core structure allowing multiple modes that also has a reduced cladding thickness needed to achieve an antiresonant structure. In this structure, the electric field component of the modes along the propagation direction experiences confinement due to the metal wires, while the radial electric field component is confined by antiresonant guidance. The combination of both of these guiding mechanisms has the potential for low loss, broadband guidance. Since this is not the ideal antiresonant structure, both because of the achievable loss and because of the impractical condition of keeping the ring suspended in air, a tube lattice structure has been investigated.

The proposed structure is shown in the inset of Fig. 8. Numerical simulations based on a fiber composed of 8 capillaries, each of which contains 100 subwavelength wires, and with a core diameter of about 5λ, shows the

potential for extremely low loss guidance in the THz region, reaching the minimum of 2.3 dB/km for λ=1 mm [Fig. 8].

The thin capillaries containing a large number of wires were fabricated. A cross-section of one of the capillaries is shown in the bottom inset of Fig. 8. In this particular sample 40 metal wires of about 100 μm in diameter are embedded in a ~400 μm thick, 3 mm diameter capillary. Six of these capillaries, 10 cm in length have been arranged to form a hybrid metamaterial antiresonant fiber, inset Fig. 8. Simulations of this fiber geometry indicate that the loss is expected to be as low as 0.3 dB/m and characterization of this waveguide is currently being performed.

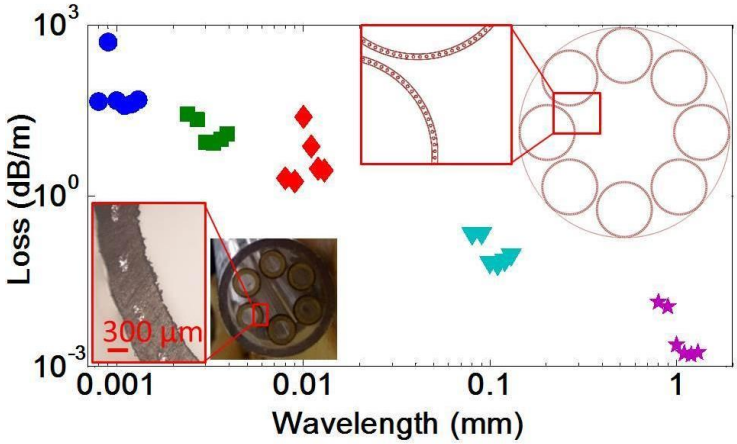

Fig. 8 Simulated loss of the hybrid antiresonant metamaterial fiber. The different symbols/colours correspond to the same structure scaled in order to have similar wavelength/size ratio in the various frequency ranges. Inset (bottom left): fabricated metamaterial antiresonant fiber and detail of the tube including metal wires. Inset (top right): the simulated structure and a detail of the tube edge [55].

3.3 Air-core waveguides with magnetic resonators cladding

Metamaterial based waveguides offer unprecedented control of electromagnetic waves, including guiding due to electric and magnetic resonances. To explore the range of achievable properties, we have characterized an air-core planar waveguide with a metamaterial cladding consisting of arrays of split-ring resonators at THz frequencies [60]. Each side of the waveguide consists of an array of ~140 fibers, each ~4.6cm long, as represented by the schematic of Fig. 9(a). The guiding mechanism of such a waveguide depends on the polarization and propagation direction of the radiation, i.e. total internal reflection due to the magnetic response (refractive indices below unity) or the electric response (metallic reflection).

There are two ways to excite the magnetic response of the SRR: a magnetic field ***H*** with a component parallel to the SRRs axis [61] or an electric field ***E*** with a component across the slot of the SRR [62, 63], as presented in Fig. 9(b). In the vicinity of the resonance frequency, the effective permeability and magnetoelectric coupling have a maximum imaginary part and strong variation in the real part, leading to a strong impedance mismatch between air and the SRR array. As a result, when an SRR array is excited with a plane wave travelling

orthogonally to the fiber axis, there will be a sharp drop in the transmittance at the resonance. The plasmonic response of the SRR array can be excited when the electric field ***E*** has a component parallel to the SRRs axis: Due to the longitudinal invariance of the SRRs, in this orientation the SRR array is equivalent to a wire array, exhibiting metallic behaviour. For frequencies below the effective plasma frequency (a function of spacing and diameter of the "wires"), the array exhibits negative permittivity resulting in metallic reflection, while at higher frequencies it effectively behaves as a dielectric. Directional invariance, along the length, results in spatial dispersion of the SRR array. Therefore, with increasing wavevector component along the axis of array, the dip due to resonant response and the plasma frequency both shift to higher values.

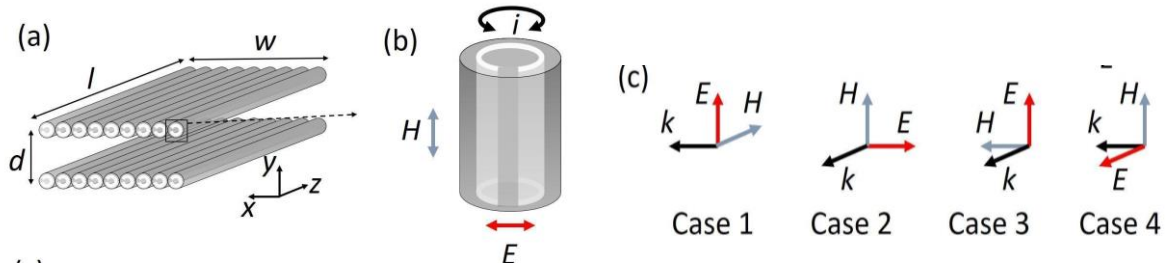

Fig. 9 (a) Schematic of the air-core waveguide with SRRs arrays as cladding. (b) Illustration of the electric and magnetic field components that can excite the magnetic resonance in a SRR resulting in the indicated current *i*. (c). Investigated propagation and polarization configurations, relative to the waveguide as shown in (a), [60].

Waveguides bounded by two parallel SRR arrays can be used in four different combinations of polarization and wave propagation direction, with substantially different properties [Fig. 9(c)]. The most interesting case occurs when the propagation direction is perpendicular to the axis of the SRRs, the magnetic field is perpendicular to the SRRs cross-section plane and the electric field has a component across the slot leading to excitation of the magnetic resonance with no spatial dispersion (as the wavevector component along the SRRs vanishes). The measured transmittance in this configuration [Fig. 10(a)] has a peak in transmission at 164 GHz, which corresponds to the magnetic resonance of the SRR arrays. The relatively high transmission between 160 GHz and 230 GHz can be explained in terms of the effective refractive index and impedance of the cladding. Around the magnetic resonance the refractive index drops below one, causing total internal reflection from the hollow core. This is accentuated by the impedance mismatch between the SRR plates and air, leading to strong reflection. The numerical simulation [Fig. 10(b)] confirms the dominant part of the power is confined between the two plates and the existence of a strong magnetic response (the field in the resonators opposes the field in the core). In other cases, weak excitation of the magnetic response, or guidance due to the presence of plasmonic resonances have been observed. This example of a waveguide clad by magnetic resonators illustrates the variety of guidance mechanisms metamaterials can provide. Careful design could provide useful devices for dispersion management and filtering in integrated THz devices.

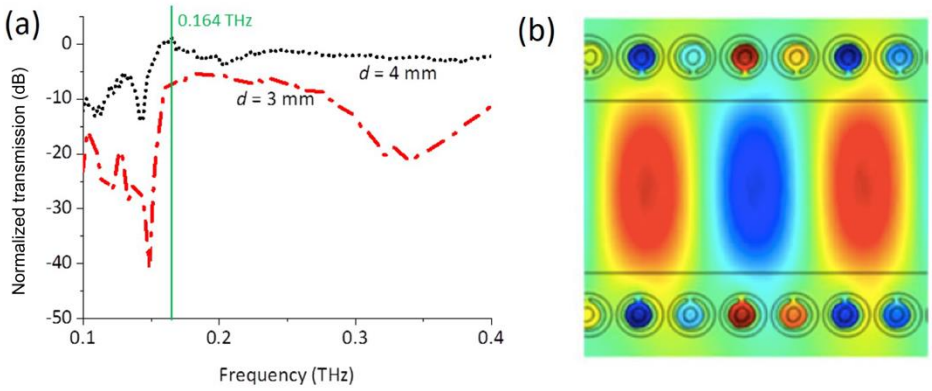

Fig. 10 (a) Transmittance of waveguides measured for various core sizes (propagation direction perpendicular and magnetic field parallel to SRR axis, electric field with component across the SRR slot). Green solid line: resonance frequency. (b) Simulated *z*-component (along the SRR axis) of the magnetic field at the magnetic resonance frequency. [60].

4. Sub-diffraction imaging

Wire metamaterials offer a new paradigm to beat the optical diffraction limit by converting evanescent waves to propagating waves of constant phase velocity [10]. WMMs act as a sub-diffraction-limited endoscope in which the propagating waves carry subwavelength features from the object plane to an image plane at the opposite side of the medium. Employing fiber drawing techniques, we fabricated WMMs with straight, tapered and prism shapes for THz frequencies. We experimentally demonstrated that our fabricated magnifying and non-magnifying hyperlenses can be used for focusing with resolution up to λ/28 in the near-field [29] and up to λ/13 in the far-field [64] at THz frequencies. Compared to other techniques proposed for THz sub-diffraction imaging, WMM hyperlenses enjoy relatively low losses: at the lower frequency end of the THz spectrum our tapered hyperlens could focus light to subwavelength focal spots with no measurable loss increase compared to the loss of the dielectric.

We experimentally demonstrated that a straight hyperlens can be used to resolve features as small as λ/27. The straight hyperlens (L=1.5 mm) was placed in front of a double aperture (200 μm apertures separated by 100 μm) and the field was measured directly after the hyperlens [Fig. 11]. Good low-frequency images are obtained at Fabry-Perot resonances (FPRs).

We also experimentally demonstrated that a tapered hyperlens can be used for focusing and magnification purposes. For the experiment a 1 mm aperture was placed in front of the larger end of a tapered hyperlens, and the near-field radiation was measured at the narrow end of the taper for two scenarios: once without the hyperlens, measuring near-field directly after the aperture [Figs. 12(a) and 12(b)] and once with the hyperlens, measuring near-field directly after the hyperlens [Figs. 12(c) and 12(d)], for comparison. For a x-polarised linear THz excitation a field distribution strongly focused along the x-direction was observed, with full-width at half-maximum (FWHM) of λ/28. The focusing occurs in the same direction of the input polarization where

extraordinary, non-diffracting waves are supported, while the perpendicular direction supports ordinary waves, which are diffracting.

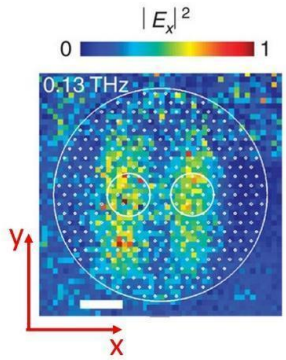

Fig. 11 *x*-polarized electric field intensity at 0.13 THz for a double aperture measured after propagation through a wire array fiber of 1.5 mm in length. Scale bar: 0.2 mm [29].

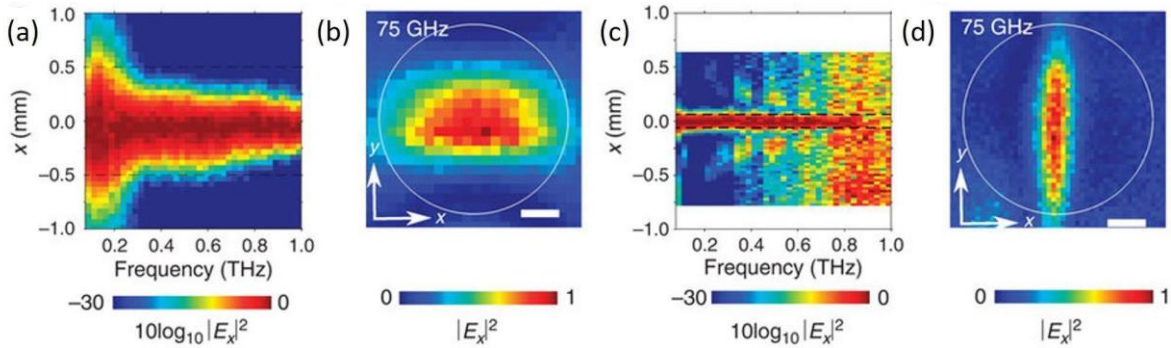

Fig. 12 (a) Intensity along x at y=0 after a 1 mm aperture. Black dashed lines show the position of the aperture. (b) Intensity at 75 GHz at aperture output. (c) Intensity along x averaged over y=0±100 μm of the tapered hyperlens output. Black dashed lines show the expected reduction of aperture size. (d) Intensity profile at 75 GHz. The aperture is shown by white circle and the scale bar is 0.2 mm in parts (b) and (d) [29].

Such wire arrays operate well at Fabry-Perot resonances (FPRs) where amplitude and phase are mostly independent of spatial frequency, leading to high quality images being transmitted to the image plane. However, away from the FPRs, images deteriorate due to resonant enhancement of evanescent waves at certain spatial frequencies resulting in image artefacts, as shown in Fig. 13(a) [65–71]. Two different techniques were proposed to overcome this restriction and allow the hyperlens to have better images over wide frequency ranges. One approach was using ultra-short electromagnetic pulses and temporal gating to filter out reflections within the slab, which cause the resonant artefacts [60]. In another approach, we applied numerical post processing, i.e. spectral convolution [Fig. 13(b)], field averaging [Fig. 13(c)], and power averaging [Fig. 13(d)], to remove imaging artefacts over a wide frequency range [72]. Another source of artefacts is direction-dependent ordinary TE waves which contribute to broadening of the point spread function [67–71]. We have shown that a projection

in spatial Fourier space can effectively filter out all ordinary waves, leading to considerable reduction in image distortion [72].

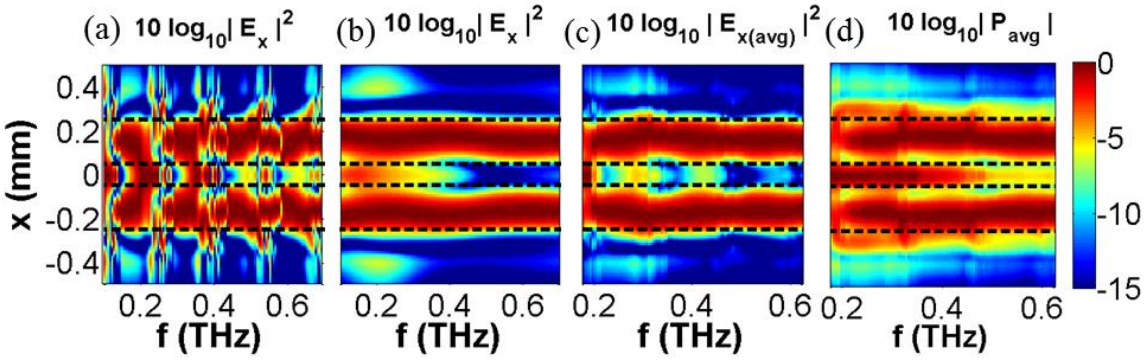

Fig. 13 (a) Simulated field intensity of two 200 μm diameter apertures with 100 μm inner-edge separation as a function of position and frequency. Same as (a) after (b) convolving field with the sinc function, (c) field average, and (d) power average over a full spectral range [72].

While our initial work only used near-field imaging to characterize hyperlenses, arguably the most exciting property of hyperlenses is their ability to convert high spatial frequencies encoding subwavelength features that are confined to evanescent waves to low spatial frequencies, which can propagate and be detected in the far-field. We have recently demonstrated that tapered WMMs can indeed be used to achieve subwavelength imaging in the far-field at THz frequencies, in two different configurations. In a first experiment, a sub-wavelength double aperture [200 μm apertures separated by 100 μm, same as used in focusing experiment, see Fig. 14(a)] was placed on the small end of a tapered hyperlens, and illuminated in transmission. Figures 14(b) and 14(c) show the measured intensity at 0.249 THz (λ=1.22 mm) for a double aperture without and with the hyperlens, respectively, as imaged by a high performance, symmetric pass far-field lens and detector (NA=1, focal length=25mm) scanned in the focal plane. The two apertures being separated by λ/12 cannot be resolved without hyperlens, but are readily distinguished with the hyperlens between the apertures and far-field lens.

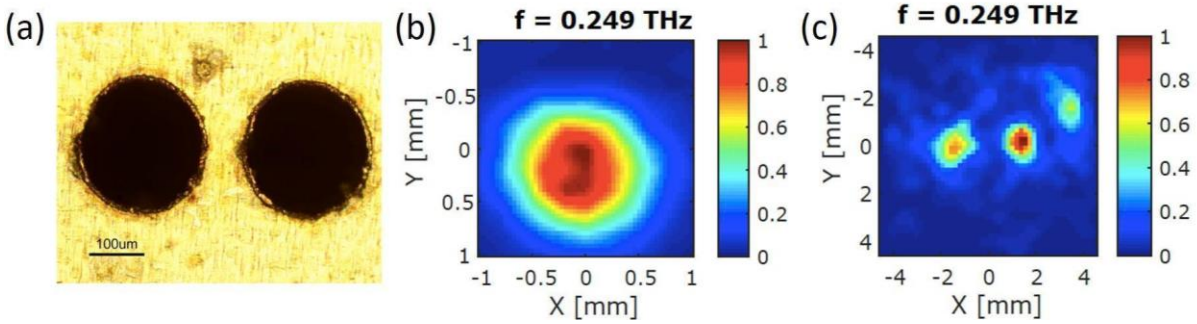

Fig. 14 (a) Microscope image of double aperture on metal disk. (b) Image of a double aperture using conventional lenses at 0.249 THz. (c) Magnified image of a double aperture using magnifying tapered hyperlens at 0.249 THz.

In a second experiment, the tapered WMM was used in reflection, so that it serves a dual purpose: The THz signal is focused through the WMM onto the sample (increasing energy density), while the reflected beam is magnified through the WMM and directed to the far-field detector. The sample is then scanned in front of the hyperlens. This is comparable to scanning optical near field microscopes, where the coupling from near field, evanescent waves to far field is done using a sharp tip or apertures, but with a much increased coupling efficiency. This allows one to turn any THz far-field system into a near-field scanner, simply by adding the tapered WMM, with reasonably high signal-to-noise ratio (25 dB in this case).

The resolution was further demonstrated using an object patterned with 19 copper lines, where the line thickness and spacing decrease from left (1 mm) to right (100 μm), The normalized intensity at 0.22 THz at different positions obtained along the sample without and with hyperlens are shown in Fig. 15(a) and 15(b). The hyperlens could resolve every line for the entire frequency range between 0.2-0.3 THz, corresponding to a resolution of less than 100 μm (λ/13).

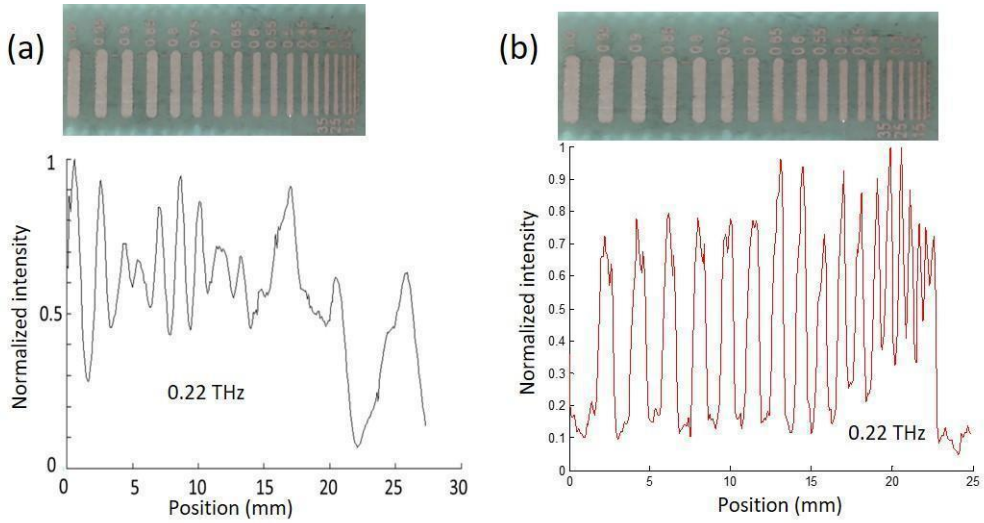

Fig. 15 Normalized intensity for a line scan at 0.22 THz (a) without and (b) with metamaterial hyperlens. Top of the figure: the imaged sample [64].

5. Conclusion and discussion

In summary, we have reviewed the most recent results in fiber drawn metamaterials for THz applications, i.e. hollow core waveguides and hyperlenses for imaging and focusing. The fundamental elements in these devices were fiber drawn wire arrays and split-ring resonators. This approach can be used to fabricate metamaterials which can be employed to manipulate both permittivity and permeability, using wire arrays and split-ring resonators respectively. We have shown how this technique is appropriate for the entire THz spectrum. Moreover, this technique allows for the realization of metamaterials which, instead of having a fixed response, are tunable. Choice of materials appears to impose a practical lower limit to the size of the realized structures with polymers, however a change of materials allows for further scaling extending the working frequency range

of drawn metamaterials to the entire IR. The fundamental meta-atoms have been exploited for several applications. We elaborated on three different types of hollow core waveguides with metamaterial cladding: the wire metamaterial cladding enables flexibility and widening of the single mode operating range for a wavelength sized core and, combined with antiresonant guidance, promises extremely low loss and broadband waveguides; parallel plates, made of split-ring resonators, providing electric and magnetic resonances, proved to confine THz radiation in a hollow core by various guiding mechanisms. Moreover, we reported experimental demonstration of WMM hyperlenses for near- and far-field THz imaging. The straight hyperlens was used to resolve features as small $\lambda/27$ and the tapered hyperlens can focus/magnify features as small $\lambda/28$.

The development of fiber drawn metamaterials appears to have reached the level of maturity required for practical applications. Perfecting the drawing and expanding the portfolio of materials will allow the use of this technique for applications in a very broad spectral range (from microwaves to the near-IR). Moreover, it is possible to exploit the metal structure not only in passive devices (as waveguides and imaging devices), but also for active and tunable devices. Creating small structures for long wavelengths in a simple and effective way will hopefully make the THz frequency region seem closer to the shorter wavelength part of the spectrum than it feels like today.

Acknowledgement

The work was supported in part by Australian Research Council (ARC) Centre of Excellence scheme CUDOS (CE110001018), and ARC under the Discovery Early Career Project Award number DE140100614 and Discovery Project DP140104116. This work was performed in part at the Optofab node of the Australian National Fabrication Facility (ANFF), using NCIRS and NSW State Government funding. A.S. acknowledges support of the Eugen Lommel Stipend and Marie Sklodowska-Curie grant of the European Union's Horizon 2020 research and innovation programme (708860).

References:

[1] M. Tonouchi, Nat. Photon. 1, 97 (2007).

[2] P. U. Jepsen, D. G. Cooke, M. Koch, Laser Photon. Rev. 5, 124 (2011).

[3] R. D. Averitt, A. J. Taylor, J. Phys. Condens. Matter 14, R1357 (2002).

[4] B. Ferguson and X. C. Zhang, Nat. Mater. 1, 26 (2002).

[5] M. Nagel, M. Först, H. Kurz, J. Phys. Condens. Matter 18, S601-S618 (2006).

[6] H. T. Chen, J. F. O'Hara, A. K. Azad, A. J. Taylor, Laser Photon. Rev. 5, 513 (2011).

[7] W. Withayachumnankul, D. Abbott, IEEE Photon. J. 1, 99 (2009).

[8] D. R. Smith, J. B. Pendry, M. C. Wiltshire, Science 305, 788 (2004).

[9] D. Schurig, J. J. Mock, B. J. Justice, S. A. Cummer, J. B. Pendry, A. F. Starr, D. R. Smith, Science 314, 977 (2006).

[10] G. Shvets, S. Trendafilov, J. B. Pendry, A. Sarychev, Phys. Rev. Lett. 99, 053903 (2007).

[11] S. Jahani, Z. Jacob, Optica 1, 96 (2014).

[12] D. Wu, N. Fang, C. Sun, X. Zhang, W. J. Padilla, D. N. Basov, D. R. Smith, S. Schultz, Appl. Phys. Lett. 83, 201 (2003).
[13] B. D. F. Casse, H. O. Moser, L. K. Jian, M. Bahou, O. Wilhelmi, B. T. Saw, P. D. Gu, J. Phys.: Conf. Ser. 34, 885 (2006).
[14] J.R. Wendt, D.B. Burckel, G.A. Ten Eyck, A.R. Ellis, I. Brener, and M.B. Sinclair, J. Vac. Sci. Technol. B 28, C6O30-C6O33 (2010).
[15] A. Reyes-Coronado, M.F. Acosta, R.I. Merino, V.M. Orera, G. Kenanakis, N. Katsarakis, M. Kafesaki, C. Mavidis, J.G. de Abajo, E.N. Economou, and C.M. Soukoulis, Opt. Express 20, 14663-14682 (2012).
[16] P. Russell, Science 299, 358 (2003).
[17] A. Argyros, J. Lightwave Technol. 27, 1571 (2009).
[18] G. F. Taylor, Phys. Rev. 23, 655 (1924).
[19] I. W. Donald, B. L. Metcalfe, J. Mater. Sci. 31, 1139 (1996).
[20] J. Hou, D. Bird, A. George, S. Maier, B.T. Kuhlmey, and J.C. Knight, Opt. Express 16, 5983-5990 (2008).
[21] A. Argyros, ISRN Optics 2013, 785162 (2013).
[22] K. Cook, J. Canning, S. Leon-Saval, Z. Reid, M. Hossain, J. Comatti, Y. Luo, and G. Peng, Opt. Lett. 40, 3966-3969 (2015).
[23] D.R. Smith and D. Schurig, Phys. Rev Lett. 90, 077405-077405 (2003).
[24] A. Poddubny, I. Iorsh, P. Belov, and Y. Kivshar, Nat. Photon. 7, 948-957 (2013).
[25] A. Tuniz, B. T. Kuhlmey, R. Lwin, A. Wang, J. Anthony, R. Leonhardt, S. C. Fleming, Appl. Phys. Lett. 96, 191101 (2010).
[26] O. T. Naman, M. R. New-Tolley, R. Lwin, A. Tuniz, A. H. Al-Janabi, I. Karatchevtseva, S. C. Fleming, B. T. Kuhlmey, A. Argyros, Adv. Opt. Mater. 1, 971 (2013).
[27] A. Tuniz, R. Lwin, A. Argyros, S. C. Fleming, B. T. Kuhlmey, J. Vis. Exp. 68, e4299 (2012).
[28] Lord Rayleigh Sec. R.S, Philos. Mag. 34, 145 (1892).
[29] A. Tuniz, K. J. Kaltenecker, B. M. Fischer, M. Walther, S. C. Fleming, A. Argyros, B. T. Kuhlmey, Nat. Commun. 4, 2706 (2013).
[30] A. Tuniz, R. Lwin, A. Argyros, S. C. Fleming, E. M. Pogson, E. Constable, R. A. Lewis, and B. T. Kuhlmey, Opt. Express 19, 16480 (2011)
[31] N. Singh, A. Tuniz, R. Lwin, S. Atakaramians, A. Argyros, S. C. Fleming, and B. T. Kuhlmey, Opt. Mater. Express 2, 1254 (2012).
[32] A. Wang, A. Tuniz, P. G. Hunt, E. M. Pogson, R. A. Lewis, A. Bendavid, S. C. Fleming, B. T. Kuhlmey, and M. C. J. Large, Opt. Mater. Express 1, 115 (2011).
[33] A. Tuniz, B. Pope, A. Wang, M. C. J. Large, S. Atakaramians, S. Min, E. M. Pogson, R. A. Lewis, A. Bendavid, A. Argyros, S. C. Fleming, and B. T. Kuhlmey, Opt. Express 20, 11924 (2012)
[34] S. Fleming, A. Stefani, X. Tang, A. Argyros, D. Kemsley, J. Cordi, R. Lwin, arXiv:1703.07032 (2017).
[35] http://www.cue-inc.com/Polyurethane-Data-Sheet.pdf
[36] J. G. Hayashi, S. Fleming, B. T. Kuhlmey, and A. Argyros, Opt. Express 23, 29867 (2015).

[37] J. G. Hayashi, R. Lwin, A. Stefani, S. Fleming, A. Argyros, B. T. Kuhlmey, in 41st International Conference on Infrared, Millimeter, and Terahertz waves (IRMMW-THz), Copenhagen, 2016, pp. 1-2.
[38] A. Barh, B. P. Pal, G. P. Agrawal, R. K. Varshney, B. M. A. Rahman, IEEE J. Sel. Top. Quantum Electron. 22, 365 (2016).
[39] A. Markov, H. Guerboukha, M. Skorobogatiy, J. Opt. Soc. Am. B 31, 2587 (2014).
[40] S. Atakaramians, S. Afshar V, T. M. Monro, D. Abbott, Adv. Opt. Photonics 5, 169 (2013).
[41] K. Wang, D. M. Mittleman, Nature 432, 376 (2004).
[42] G. Gallot, S. P. Jamison, R. W. McGowan, D. Grischkowsky, J. Opt. Soc. Am. B 17, 851 (2000).
[43] M. Navarro-Cía, J. E. Melzer, J. A. Harrington, O. Mitrofanov, J. Infrared Millim. Terahz. Waves 36, 542 (2015).
[44] J.-Y. Lu, C.-P. Yu, H.-C. Chang, H.-W. Chen, Y.-T. Li, C.-L. Pan, C.-K. Sun, Appl. Phys. Lett. 92, 064105 (2008).
[45] H. Bao, K. Nielsen, O. Bang, P. U. Jepsen, Sci. Rep. 5, 7620 (2015).
[46] N. Yudasari, J. Anthony, R. Leonhardt, Opt. Express 22, 26042 (2014).
[47] J. Anthony, R. Leonhardt, S. G. Leon-Saval, and A. Argyros, Opt Express 19, 18470 (2011).
[48] S. Atakaramians, A. Argyros, S. C. Fleming, B. T. Kuhlmey, J. Opt. Soc. Am. B 29, 2462 (2012).
[49] S. Atakaramians, A. Argyros, S. C. Fleming, B. T. Kuhlmey, J. Opt. Soc. Am. B 30, 851 (2013).
[50] M. Yan, N. A. Mortensen, Opt. Express 17, 14851 (2009).
[51] S. Atakaramians, B. T. Kuhlmey, Opt. Lett. 41, 3379 (2016).
[52] H. Li, S. Atakaramians, B. T. Kuhlmey, Proc. SPIE 8205, 96680H (2015).
[53] H. Li, S. Atakaramians, R. Lwin, X. Tang, Z. Yu, A. Argyros, B. T. Kuhlmey, Optica 3, 941 (2016).
[54] H. Li, G. Ren, S. Atakaramians, B. T. Kuhlmey, S. Jian, Opt. Lett. 41, 4004 (2016).
[55] A. Stefani, R. Lwin and A. Argyros, in 41st International Conference on Infrared, Millimeter, and Terahertz waves (IRMMW-THz), Copenhagen, 2016, pp. 1-2.
[56] N. M. Litchinitser, A. K. Abeeluck, C. Headley, B. J. Eggleton, Opt. Lett. 27, 1592 (2002)
[57] Francesco Poletti, Opt. Express 22, 23807 (2014)
[58] V. Setti, L. Vincetti, A. Argyros, Opt. Express 21, 3388 (2013)
[59] A. L. S CruzI, V Serrao, C. L Barbosa, M. A. R Franco, C. M. B Cordeiro, A. A Argyros, X. Tang, J. Microwaves. Optoelectron. Electromagn. Appl. 14, 45 (2015).
[60] X. Tang, B. T. Kuhlmey, A. Stefani, A. Tuniz, S. C. Fleming, A. Argyros, J. Lightwave Technol. 34, 5317 (2016).
[61] W. N. Hardy, L. A. Whitehead, Rev. Sci. Instrum. 52, 213 (1981).
[62] P. Gay-Balmaz, O. J. F. Martin, J. Appl. Phys. 92, 2929 (2002).
[63] N. Katsarakis, T. Koschny, M. Kafesaki, E. N. Economou, C. M. Soukoulis, Appl. Phys. Lett. 84, 2943 (2004).
[64] X. Tang, B. Kuhlmey, A. Tuniz, S. Fleming, A. Argyros, in *Photonics and Fiber Technology 2016 (ACOFT, BGPP, NP)*, OSA Technical Digest (online) (Optical Society of America), 2016, paper ATh3C.4.

[65] A. Tuniz, D. Ireland, L. Poladian, A. Argyros, C. Martijn de Sterke, B. T. Kuhlmey, Opt. Lett. 39, 3286 (2014).

[66] K. J. Kaltenecker, A. Tuniz, S. C. Fleming, A. Argyros, B. T. Kuhlmey, M. Walther, B. M. Fischer, Optica 3, 458 (2016).

[67] A. Tuniz, B. T. Kuhlmey, Sci. Rep. 5, 17690 (2015).

[68] P. A. Belov, Y. Zhao, S. Sudhakaran, A. Alomainy, Y. Hao, Appl. Phys. Lett. 89, 262109 (2006).

[69] M. G. Silveirinha, P. A. Belov, C. R. Simovski, Phys. Rev. B 75, 035108 (2007).

[70] X. Li, S. He, Y. Jin, Phys. Rev. B 75, 045103 (2007).

[71] R. Kotynski, T. Stefaniuk, J. Opt. A 11, 015001 (2009).

[72] M.S. Habib, A. Tuniz, K.J. Kaltenecker, Q. Chateiller, I. Perrin, S. Atakaramians, S.C. Fleming, A. Argyros, B.T. Kuhlmey, Opt. Express 24, 17989 (2016).